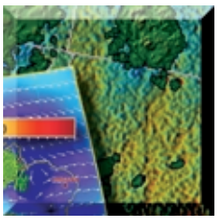

Extracting Fine-Scale Wind Fields from Synthetic Aperture Radar Images of the Ocean Surface

Pierre D. Mourad, Donald R. Thompson, and Douglas C. Vandemark

Work is described whose long-term goal is the extraction and analysis of fine-scale wind fields from synthetic aperture radar (SAR) images of the ocean surface. Results are based on a field experiment in which a SAR image was taken nearly simultaneously with *in situ* aircraft-based turbulence and radar altimeter measurements. These results show a direct correlation between SAR "streaks" and atmospheric roll vortices. They also show that rolls generate mesoscale variability in the surface wave spectrum, implying that SAR streaks are due to ocean surface roughness elements created by both the instantaneous and time-averaged multiscale wind field. We are using these results to refine an analysis aimed at transforming radar backscatter into fine-scale marine mean wind speed. (Keywords: Atmospheric boundary-layer turbulence, Atmospheric roll vortices, Radar altimeter, Synthetic aperture radar.)

INTRODUCTION

A review of the research literature[1] demonstrates that a variety of atmospheric phenomena can be manifested in synthetic aperture radar (SAR) images of the ocean surface. To understand how this occurs and how the information can be used, we briefly review radar backscatter issues and then present a case study.

Measurements of satellite-based, vertically polarized radar backscatter from the ocean surface can be translated via empirical formulas into wind speed and direction. (See Ref. 2 and references therein for various CMOD or C-band modulation algorithms that relate wind speed and backscatter for 5.3-GHz C-band scatterometers.) This relationship exists because the wind roughens the water surface via the production of gravity-capillary waves,[3–5] which in turn effectively backscatter radar signals via Bragg scattering for grazing angles between 20 and 70°.[6] (Gravity-capillary waves are temporally and spatially periodic disturbances of the ocean surface on scales of approximately 1 to 30 cm whose restoring force is a combination of gravity and surface tension.) "Parasitic" gravity-capillary waves (i.e., waves whose growth is predicated on the underlying wave field rather than the wind) may also be generated by the roughening of the front face of wind-driven gravity waves that are near breaking. (Jessup et al.[7] review the literature on gravity-capillary waves and also offer infrared images of their microscale breaking.)

These waves can be an additional significant source of direct C-band radar backscatter[8] for grazing angles between 60 and 10° and smaller.[9] They can also induce

multiple scattering.[10,11] Furthermore, small-scale bores (also known as "microbores"; think of centimeter-scale breaking waves) created by roughening gravity waves are a significant source of backscatter at low grazing angles.[10]

Parasitic gravity-capillary waves and microbores are independent of local, short-term wind conditions. So are large-scale gravity waves and swell, which modulate the gravity-capillary wave field, thereby producing significant variations in radar backscatter.[12] For wind speeds of only a few meters per second, the amplitude of the gravity-capillary waves eventually saturates. For winds at and above the saturation speed, however, continued momentum flux into the air–sea interface causes the underlying longer-wavelength surface waves to increase in amplitude on scales greater than or equal to tens of seconds. Such an increase induces tilting in the gravity-capillary wave field, which makes the ocean surface more visible (brighter) to radar. This accounts for the general increase in radar backscatter with mean wind speed.[12]

THE ONR SHOALING WAVES PILOT STUDY

As part of the Shoaling Waves Pilot Study sponsored by the U.S. Office of Naval Research (ONR) in the fall of 1997, we had a rare opportunity to compare *in situ* wind and wave data collected from a research aircraft with a co-located, nearly co-temporal SAR image. We briefly describe the instrumentation and discuss some of the relevant analysis in this section.

A light, one-person aircraft known as the National Oceanic and Atmospheric Administration/Oakridge LongEZ was flown in a square pattern off Duck, North Carolina, on 5 November 1997 (Fig. 1a). The LongEZ carried a sonic anemometer to capture 50-Hz turbulence data. At the same time, a Radarsat SAR image was captured (Fig. 1b). The area covered by the SAR image, the relative direction of the surface wind at 15 to 20 m, and the radar backscatter streaks are marked. Also included is the flight path of the LongEZ. Note that the measured wind is about 15 to 20° clockwise from the orientation of the SAR streaks, whereas predictions by the mesoscale model known as MM5 (not shown) show the wind to be 0 to 20° counterclockwise of the streaks. Streak spacing, width, and length vary from 1.3 to 2.8, 0.5 to 1.0, and 5.0 to 25.0 km, respectively.

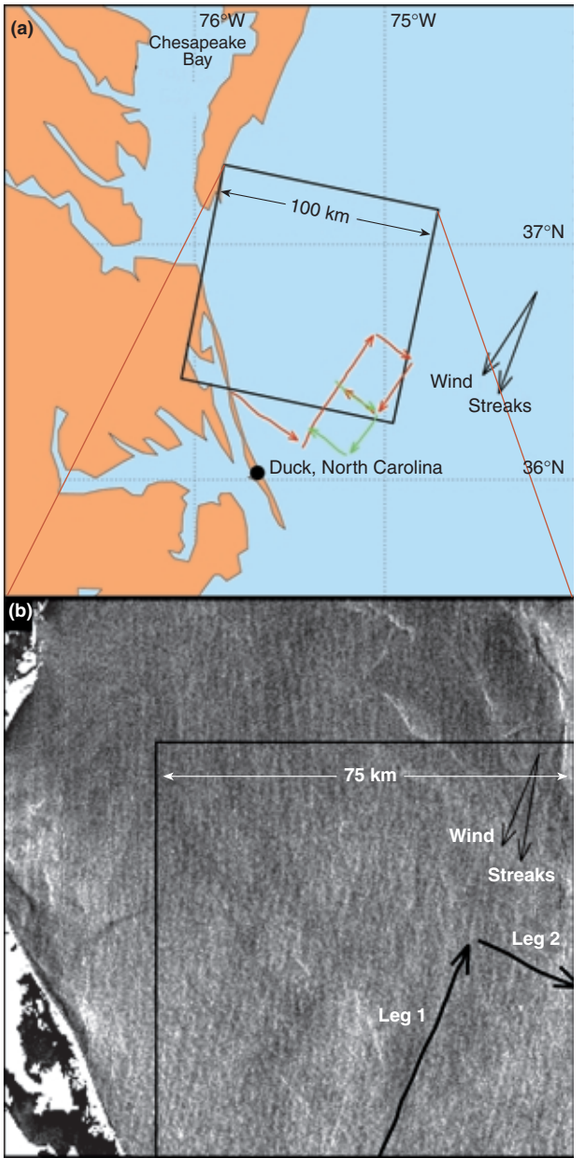

Figure 1. ONR Shoaling Waves Pilot Study experimental geometry (a) and associated Radarsat SAR image (b). The LongEZ flight path at 15 to 20 m above the water (orange arrows) and at 300 m (green arrows) are also shown. The 75-km square was used for the autocorrelation map in Fig. 2b.

Results

SAR Streaks Created by Atmospheric Turbulence

Data from the pilot study show, for the first time, that streaks in a SAR image can indeed be due to atmospheric roll vortices (see Figs. 1–3). This conclusion is based on a comparison of the spatial structure of the radar backscatter from the wind-forced ocean surface with the structure of the wind forcing. To highlight the streak structure, Fig. 2a shows the autocorrelation of the 25-km-square southeast corner of the SAR image. Evident is a central field of high correlation (the correlation of the central SAR streak with itself) with a length of approximately 10 km, paralleled on either side by elongated fields of lower correlation, the correlation of the central streak with its neighbors. (Note

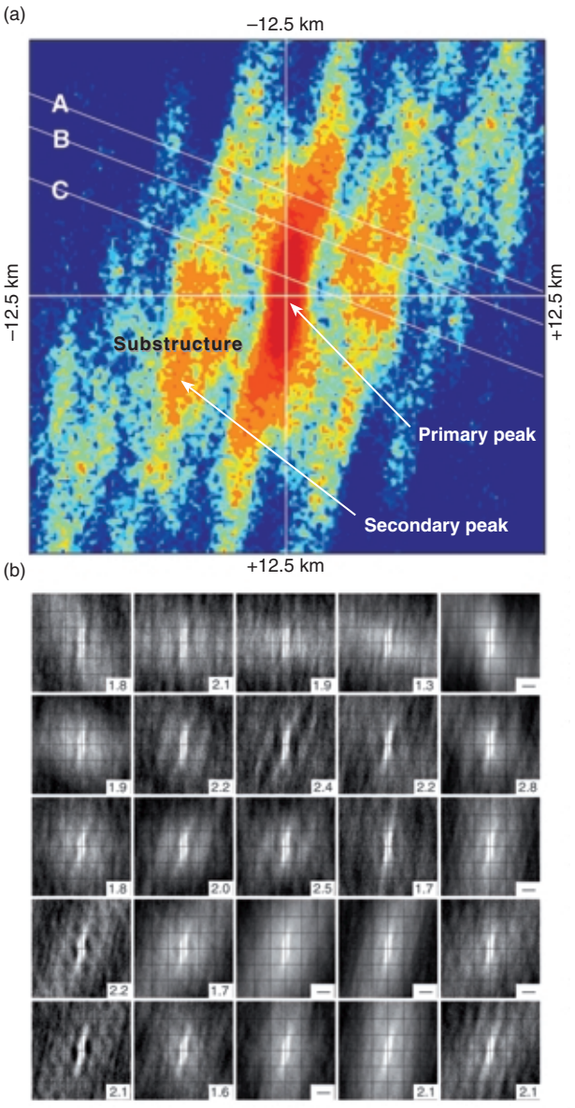

Figure 2. (a) Autocorrelation of the 25-km-square southeast corner of the SAR image shown in Fig. 1b. (b) Field of autocorrelation analysis taken from the 75-km square in the southeast corner of the image shown in Fig. 1b. Numbers in boxes give the average distance in kilometers between streak manifestations in each subimage; dashes indicate that no meaningful distance could be identified.

that the maximum off-center correlation here is insignificant, $R^2 = 0.04$. However, a one-dimensional version that averages rows of the SAR image that are *perpendicular* to the streaks yields a meaningful correlation, $R^2 = 0.40$.) Measurements along lines A, B, and C in the figure show that the distance between streak manifestations varies from 1.5 to 2.5 km, while the streak widths are about 0.5 to 1.0 km. Also note in Fig. 2a that the lengths of the secondary peaks are shorter, around 6 km, and that they each contain substructures with lengths of about 2 to 3 km. Figure 2b shows a field of autocorrelation analyses taken from the 75-km-square southeast corner of the SAR image. The average distances, as well as the scales associated with the streaks, are consistent with those shown in Fig. 2a. However, the streak length inferred by autocorrelation is an underestimate, since twists and turns in a contiguous line of enhanced backscatter are not preserved.

Figure 3 shows a wavelet analysis of the horizontal wind speed measured parallel and perpendicular to the surface wind. Figure 3a illustrates the distribution of length scales of along-track wind forcing of the ocean surface. Figure 3b illustrates across-track wind forcing as well as coherent structures in the atmospheric boundary layer. (Contributing to the portion of the spectrum denoted "gust microfronts," for example, are

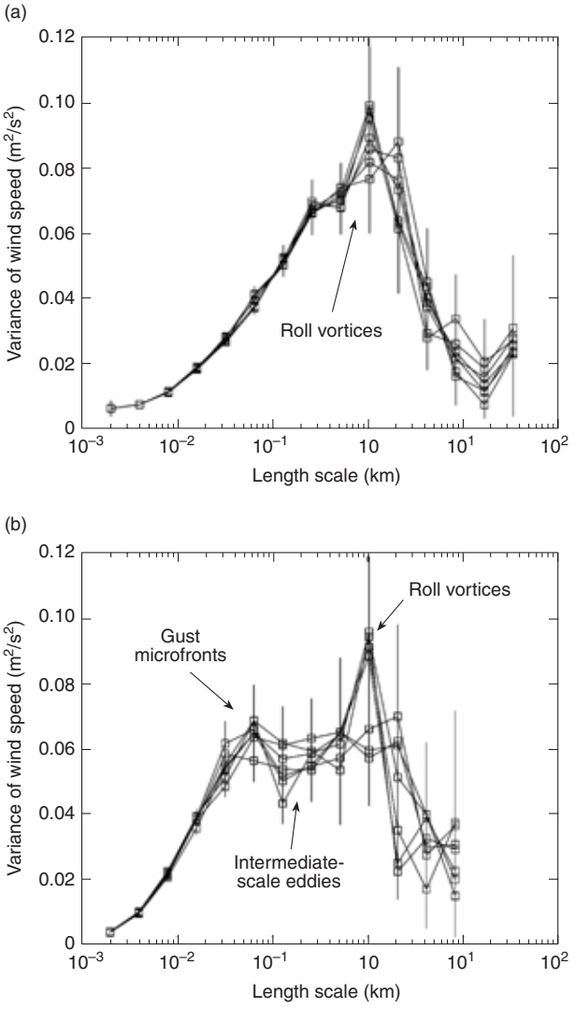

Figure 3. Wavelet analysis of horizontal wind speed versus length scale measured (a) along the flight track parallel to the local wind, and hence essentially parallel to the SAR streaks (leg 1, Fig. 1b), and (b) across the flight track perpendicular to the local wind, and hence essentially perpendicular to the SAR streaks (leg 2, Fig. 1b).

individual vertical momentum flux events of the same name. This conclusion is supported by the spectra of the vertical momentum flux, which peaks at the scale of the gust fronts [not shown].)

The dominant length scale in Fig. 3b is 1.0 km, which is on the order of the average width of the SAR streaks. However, note that the scale of the along-streak wind forcing shown in Fig. 3a is 1.0 to 3.0 km. This is comparable to the 2- to 3-km substructure shown in the autocorrelation images (Fig. 2). However, it is smaller than the streak lengths shown in the SAR image (Fig. 1b) and the central structures of the autocorrelation images, even after taking into account the 20° difference in flight direction versus streak direction. These data show that the backscatter field exhibits scales greater than or equal to those associated with the wind that generates that field. This finding suggests that the SAR streaks show the effects of both the instantaneous (order of seconds) and time-integrated (order of tens of seconds and longer) wind forcing on the ocean surface. Consistent with this interpretation is the observation that the surface wave field associated with this SAR image manifests spatial variations in surface wave slope, as discussed in the next section. Apparently, the spatial structure of the overriding atmospheric turbulence—a lineal arrangement by roll vortices of eddies with scales on the order of 1.0 km—helps create the "streak-like" signature of atmospheric roll vortices.

Atmospheric Roll Vortices Induced by Mesoscale Variability

Recent analysis by the authors and others supports the hypothesis that SAR streaks arise from spatial variability in the time-integrated response of the ocean to structured wind forcing. The analysis demonstrates, using data from the ONR Shoaling Waves Pilot Study, that 40 to 70% of the Ku-band radar altimeter variance (proportional to the mean square slope of the ocean surface) within a 1.1-m footprint is explained by comparable variations in the co-located, simultaneously measured wind speed. These variations were also found to mimic the across-streak structure visible in the SAR image. Since the mean square slope of the ocean surface is a strong function of wind forcing, this result supports the interpretation of the difference between SAR streaks and their presumed wind forcing.

Figure 4 shows a comparison of the fluctuations of the along-track component of the wind vector U_x and the inverse of the radar altimeter measurement (1/NRCS) for LongEZ flight leg 2, the leg flown across the streaks (see Fig. 1b). (NRCS refers to normalized radar cross section.) The wind and radar fluctuations (top of Figs. 4a and 4b, respectively) are reported in terms of a percentage modulation about their respective mean value. A wavelet decomposition is then applied to both U_x and (1/NRCS) using a continuous wavelet transform. The result (middle of Figs. 4a and 4b) is real wavelet coefficients that contain structural information in both wavelength (y axis) and along-track distance (x axis). These data represent the "best fit" of a harmonic at each scale, where the image contains significant energy at that scale and specified distance along the aircraft's ground track. A visual comparison of the two wavelet transforms yields meaningful similarities. A coherence function versus wavelet scale is readily computed from the two time series (top panels in Figs. 4a, 4b, and 4d). The peak of this function has a value of $R^2 = 0.6$ at a wavenumber of 1/(1500 m).

The power spectral density of the signals is provided in the bottom panels of Figs. 4a and 4b. These plots are equivalent to a Fourier spectral computation, but with the inherent filtering of the Morlet function. As noted previously, measurements were given as percentage of fluctuation. The direct spectral comparison plot (Fig. 4c) indicates that the atmospheric and surface signatures at these spatial scales (0.5 to 4.0 km) are quite similar in amplitude and shape. This is consistent with the direct comparison of the time series of the U_x and (1/NRCS) (Fig. 4d). Again, the inverse of the altimeter measurement is directly proportional to the surface mean square slope within the 1.1-m altimeter footprint. Therefore, these results show a variation in the surface wave amplitude distributed on scales similar to those of the wind forcing, consistent with the interpretation of the SAR image given previously.

Discussion

The results presented here quantitatively bolster the claim that the spatial variability of radar backscatter can be intimately tied to the spatial variability of the wind that blows on the ocean surface. We now go a step further, comparing in detail the measured horizontal wind speed along flight leg 2 of the ONR Shoaling Wave Pilot Study extracted from the 5 November 1997 SAR image. Thompson and Beal, this issue, have shown how a modified CMOD4 algorithm designed to model the relationship between radar backscatter and wind speed for horizontally polarized C-band radar can be used along with the measured mean wind direction from the LongEZ to convert this image to wind. With this algorithm we show, using the measured air–sea temperature difference (–6°C), that the measured and SAR-derived winds were within 0.2 m/s of each other.

Let us examine the wind extraction in more detail. Figure 5a compares the "predicted" and "measured" relative radar backscatter along LongEZ flight leg 2 as a function of distance for various widths of the cross-track averaging window applied to the measured backscatter. The predicted radar backscatter is derived from

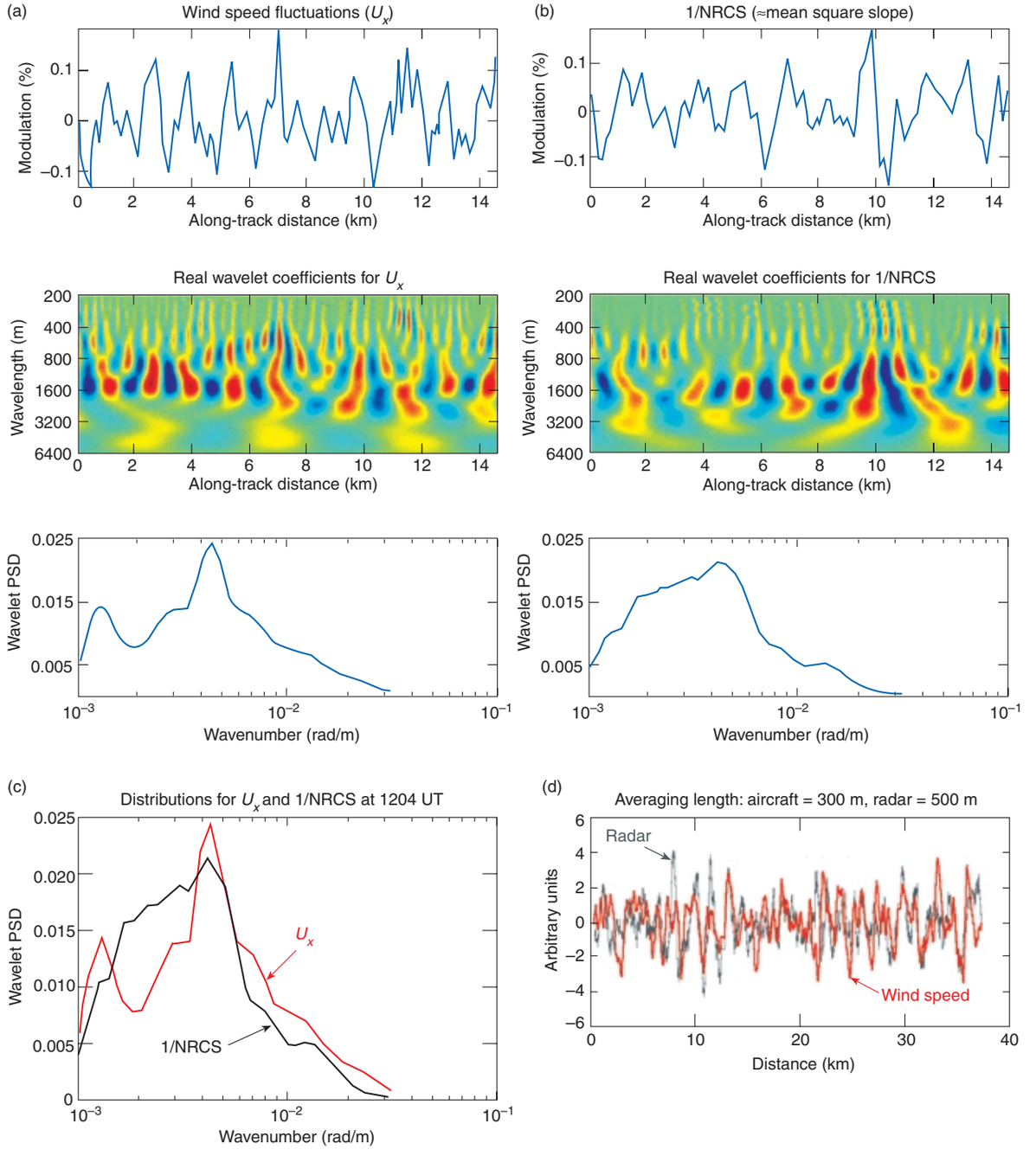

Figure 4. Results of an analysis of the fluctuations in wind (U_x) and the inverse of the radar altimeter measurement (1/NRCS) for the LongEZ flight leg at 1204 UT. See text for details. (NRCS = normalized radar cross section, PSD = power spectral density.)

the measured wind-speed time series, using the measured average wind direction and the algorithm of Thompson and Beal. The measured radar backscatter is taken along a 17.5-km range-directed swath within the SAR image underlying LongEZ flight leg 2 (see Fig. 1b). The width of the averaging window is noted on the figure. (In the middle panel of Fig. 5a, for example, the swath was 17.5 km long in range and 100 m wide in azimuth.) As the width of the cross-track averaging window is increased, the standard deviations of the measured and predicted backscatter along the entire flight leg become more similar.

This result motivated the comparison in Fig. 5b, which shows the (constant) standard deviation of the

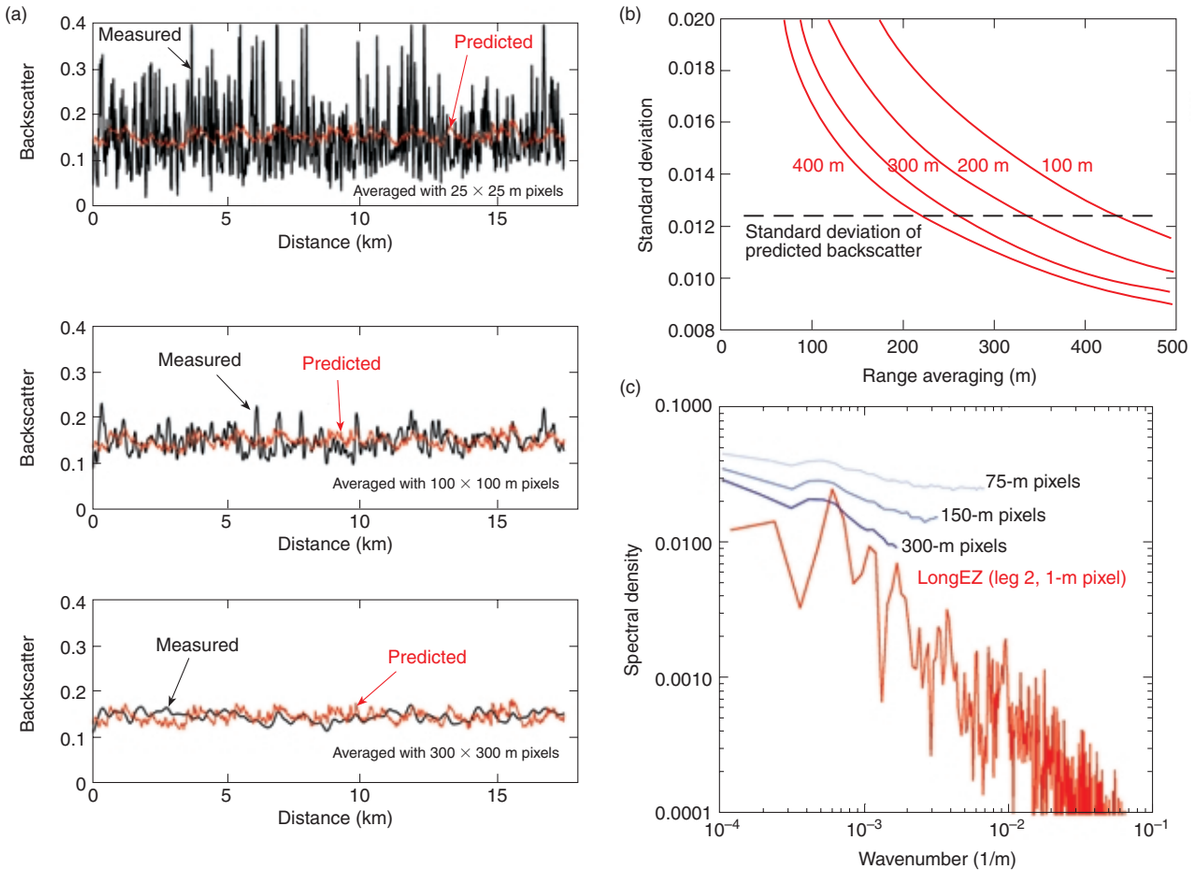

Figure 5. (a) Predicted and measured backscatter cross section along LongEZ flight leg 2 during the Shoaling Wave Pilot Study. The three panels from top to bottom show results for 25-, 100-, and 300-m cross-track averaging of the measured SAR cross section, respectively. (b) Comparison of the (constant) standard deviation of the predicted backscatter cross section along the entire LongEZ flight leg (dashed horizontal line) and those determined from swaths of various width from the underlying SAR image. The different curves are associated with different choices of averaging length in azimuth (cross-track), applied to the 17.5-km-long swath, with different choices of averaging length in range (along-track) read off the *x* axis of the plot. (c) Comparison of the power spectrum of the wind speed directly measured by the LongEZ and those predicted from a portion of the SAR wind image underlying the flight of the LongEZ and smoothed to the specified pixel dimension.

predicted backscatter cross section along the entire LongEZ flight leg and cross sections measured along swaths of various widths from the underlying SAR image. The different curves are associated with different choices of averaging length in azimuth (cross-track), applied to the 17.5-km-long swath, with different choices of averaging length in range (along-track) read off the *x* axis. (The "300-m" curve, for example, intersects the curve denoting the standard deviation of the predicted backscatter at a range of 260 m. This intersection shows that the standard deviation of the 17.5-km-long, 300-m-wide SAR swath underlying the LongEZ flight leg agrees with the value predicted from the LongEZ measurements after applying a running average in the form of a 300 × 260 m box to the SAR swath.)

Note that the standard deviation of the measured backscatter along the swath is lower than that predicted from the aircraft data for running average boxes with sides on the order of 300 m or larger. This suggests choices of averaging length one can apply to a portion of a SAR image to infer wind speed from that portion of the SAR image with a desired accuracy and precision in both the mean and standard deviation of the wind. Also note that the average length is the same scale as the "intermediate-scale eddies" shown in Fig. 3b, suggesting that contributions from those and smaller eddies to the radar backscatter must be filtered in order for the measured and predicted radar backscatter to agree. (Such a choice of averaging would also remove the influence of most long-wave swell systems, for example.)

Figure 5c compares the horizontal wind-speed power spectrum data collected by the LongEZ with the corresponding spectra computed from SAR wind estimates derived using the procedures already discussed. (The SAR wind spectra were extracted from the portion of the image enclosed by the yellow box in Fig. 3b of the Thompson and Beal article, this issue. As noted in that

article, this section of the SAR image coincides roughly with the overflight of LongEZ during leg 2, also shown on the image, about 40 min after the image was collected.) The LongEZ spectrum shown in Fig. 5c is a standard estimate of the power spectral density of the horizontal wind speed ($\sqrt{u^2 + v^2}$) as measured by the LongEZ. For leg 2, the LongEZ flight direction was normal to the surface wind direction, and hence nearly perpendicular to the atmospheric rolls and streaks seen in the SAR image. Since the LongEZ air speed was nearly constant at 50 m/s, and the velocity data were collected at a rate of 50 Hz, the assumption of spatial homogeneity allows us to infer a spatial sampling interval of 1 m.

The three SAR-derived spectra shown in Fig. 5c were extracted from the same subimage of the SAR scene. Three subimages were generated from the primary one with different choices of averaging length scale: in particular, they were sampled at resolutions of 300, 150, and 75 m. Again, as described by Thompson and Beal (this issue), these subimages were converted to wind speed using a modified CMOD4 algorithm corrected for horizontal polarization and the mean wind direction (from 50° relative to true north) along the LongEZ flight leg. The SAR-derived power spectra shown in the figure are averages of one-dimensional spectra extracted from each row of the corresponding subimage. The dc components of these spectra (not shown) give the square of the predicted wind speed. For the SAR spectra, these values are $(8.4\ \text{m/s})^2$, $(8.6\ \text{m/s})^2$, and $(8.7\ \text{m/s})^2$ for the 300-, 150-, and 75-m subimages, respectively. The square root of each of these quantities represents the mean wind speeds extracted from the SAR subimages that correspond to neutral-stability wind speeds measured 10 m above the sea surface. The actual (versus neutral equivalent) mean horizontal wind measured at 15 m during leg 2 was 7.7 m/s. The marine atmospheric boundary layer was unstable during the LongEZ observations, with an air–sea temperature difference of −6°C. After adjustment for stratification and the height of the aircraft relative to 10 m, the dc component of the LongEZ power spectrum in Fig. 5c is therefore $(8.2\ \text{m/s})^2$. This value is the square of the neutral-equivalent, 10-m wind speed corresponding to the LongEZ measurement as determined from the TOGA-COARE algorithm.[13] It is exciting that the SAR-derived and *in situ* neutral wind are so close (within 0.2 m/s) because it offers further support to the hypothesis that SAR can be used to extract fine-scale wind fields over the ocean.

Both the SAR-derived and the LongEZ-based spectra show a peak at about $k = 5 \times 10^{-4}$ (1/m) corresponding to the 1.5- to 2.0-km spacing of the atmospheric rolls seen in the SAR image. Figure 5c shows that the SAR-derived spectrum corresponding to the subimage built with the 75-m pixels is somewhat higher than the LongEZ spectrum and, in particular, that the decay rates of these two spectra are not the same. This is because fluctuations in the SAR imagery, especially at the shorter spatial scales, can be caused by complicated scattering and surface-wave hydrodynamic processes as well as by direct wind variation.

These fluctuations in the SAR imagery, which we refer to as surface-induced fluctuations, are produced, for example, by pixel-to-pixel changes in the local SAR incidence angle or by changes in the spectral density of short surface waves due to hydrodynamic modulation.[14] Surface-induced fluctuations would, in fact, be present even if the wind were constant. It is an important topic of current research to understand how to characterize and isolate these two different processes more accurately. Notice in Fig. 5c that as the SAR pixel spacing becomes larger, the high-frequency decay of the SAR spectra more closely matches that of the LongEZ wind-speed spectrum and that the magnitude of the SAR-derived spectral density at all frequencies approaches that of the LongEZ spectrum. The basic idea is that the surface-induced fluctuations result from oceanographic phenomena such as surface waves whose scales are smaller than a few hundred meters or so. Thus, smoothing the SAR over these scales should reduce the effect of surface-induced fluctuations on the total variance of the final SAR wind image.

Why are the low-frequency spans of the three SAR spectra in Fig. 5c all somewhat higher than that of the LongEZ spectrum, and why do these components depend on the SAR pixel spacing? The answers are at present not completely clear. One possible explanation is that the SAR spectra shown in the figure have not been corrected for so-called speckle noise. Speckle noise in a SAR image is related to the surface-induced fluctuations discussed previously. For an N-look SAR image with uncorrelated pixels, the speckle noise has a χ^2 probability distribution for the backscattered power with $2N$ degrees of freedom.[15] For uncorrelated pixels, the power spectrum associated with speckle noise is white, so correction for speckle would involve subtraction of a constant from the SAR spectra in Fig. 5c. This constant becomes smaller as the pixel spacing (averaging) increases. Furthermore, studies of microwave backscatter from small-footprint radars[14] have shown that the probability distribution of the backscattered power can have a tail much longer than that expected for a χ^2 distribution. It is quite probable that before the accuracy of wind-speed variance estimates from SAR imagery can be precisely assessed, a new understanding of microwave surface scattering will be required.

CONCLUSIONS

The analysis summarized here shows in detail the similarities and differences between the wind forcing of

the ocean surface and response of that surface to the wind. We now have some insight into why atmospheric roll vortices can be imaged with SAR. These vortices are often thought to be two-dimensional structures. However, this is a time-averaged view based on satellite images of clouds associated with rolls. Over short time scales, their structure is more complex than that. They are actually a lineal arrangement of instantaneous three-dimensional coherent structures with scales on the order of, or smaller than, the inversion height. This allows them to add extra momentum to parallel, along-wind portions of the ocean surface (likely close to underneath the downdrafts of the roll vortices) relative to adjacent, parallel stretches of the ocean surface (likely close to underneath the updrafts of the vortices). The ocean's response to this structured forcing is spatial variations in wave slope created by both the average and instantaneous wind forcing. These changes in surface wave slope produce mesoscale variability in radar backscatter, which produces the distinctive signature of atmospheric roll vortices in SAR images of the ocean surface.

One can average over this mesoscale structure to calculate an average radar backscatter associated with a field of atmospheric roll vortices. If one has an estimate of the average wind direction and the air–sea temperature difference, one can take remotely sensed, average backscatter and, with reasonable precision, translate it into average wind speed. Such fine-scale inferred winds are likely to be useful for improving mesoscale meteorological forecasts and assessing the wind forcing of the ocean, for example. This may prove to be a boon to those studying, living, and working in coastal zones or those whose weather comes from over the ocean, such as people living on the West Coast of United States or in Western Europe.

REFERENCES

[1]Mourad, P.D., "Footprints of Atmospheric Phenomena in Synthetic Aperture Radar Images of the Ocean Surface—A Review," Chap. 11, in *Air–Sea Exchange: Physics, Chemistry, and Dynamics*, G. L. Geernaert (ed.), Kluwer Academic Publishers, Dordrecht, pp. 269–290 (1999).

[2]Stoffelen, A., "Toward the True Near-Surface Wind Speed: Error Modeling and Calibration Using Triple Collocation," *J. Geophys. Res.* **103**, 7755–7756 (1998).

[3]Dorman, C. E., and Mollo-Christensen, E., "Observation of the Structure on Moving Gust Patterns over a Water Surface ('Cat's Paws')," *J. Phys. Oceanogr.* **3**, 120–132 (1973).

[4]Kahma, K. K., and Donelan, M. A., "A Laboratory Study of the Minimum Wind Speed for Wind Wave Generation," *J. Fluid Mech.* **192**, 339–364 (1987).

[5]Caulliez, G., Ricci, N., and Dupont, R., "The Generation of First Visible Wind Waves," *Phys. Fluids* **10**, 757–759 (1998).

[6]Plant, W. J., "Bragg Scattering of Electromagnetic Waves from the Air/Sea Interface," in *Surface Waves and Fluxes, Vol. II—Remote Sensing*, G. L. Geernaert and W. J. Plant (eds.), Kluwer Academic Publishers, pp. 41–108 (1990).

[7]Jessup, A. T., Zappa, C. J., and Yeh, H., "Defining and Quantifying Microscale Wave Breaking with Infrared Imagery," *J. Geophys. Res.* **102**, 23,145–23,153 (1997).

[8]Plant, W. J., "A Model for Microwave Doppler Sea Return at High Incidence Angles: Bragg Scattering from Bound, Tilted Waves," *J. Geophys. Res.* **102**, 21,131–21,146 (1997).

[9]Smith, M. J., Poulter, E. M., and McGregor, J. A., "Doppler Radar Measurements of Wave Groups and Breaking Waves, *J. Geophys. Res.* **101**, 14,269–14,282 (1996).

[10]Trizna, D. B., "Model for Brewster Angle Damping and Multipath Effects on the Microwave Radar Sea Echo at Low Grazing Angles," *IEEE Trans. Geosci. Remote Sens.* **35**, 1232–1244 (1997).

[11]Trizna, D. B., and Carlson, D. J., "Studies of Dual Polarized Low Grazing Angle Radar Sea Scatter in the Nearshore Regions," *IEEE Trans. Geosci. Remote Sens.* **34**, 747–757 (1996).

[12]Donelan, M. A., and Pierson, W. J., Jr., "Radar Scattering and Equilibrium Ranges in Wind Generated Waves with Application to Scatterometry," *J. Geophys. Res.* **92**, 4971–5029 (1987).

[13]Fairall, C. W., Bradley, E. F., Rogers, D. P., Edson, J. B., and Young, G. S., "Bulk Parameterization of the Air–Sea Fluxes for Tropical Ocean-Global Atmosphere Coupled-Ocean Atmosphere Response Experiment," *J. Geophys. Res.* **101**, 3747–3764 (1996).

[14]Thompson, D. R., and Gotwols, B. L., "Comparisons of Model Predictions for Radar Backscatter Amplitude Probability Density Functions with Measurements from SAXON," *J. Geophys. Res.* **99**, 9725–9739 (1994).

[15]Monaldo, F. M., "On the Use of Speckle Statistics for the Extraction of Ocean Wave Spectra from SAR Imagery," in *Proc. 1988 Int. Geoscience and Remote Sensing Symp.*, IEEE 88CH-2497-6, pp. 133–135 (1988).

ACKNOWLEDGMENTS: The authors gratefully acknowledge Timothy Crawford, who flew the NOAA/Oakridge LongEZ, and Christopher Vogel, who processed and analyzed some of the data from that flight. In addition, we thank Jielun Sun of the National Center for Atmospheric Research and Larry Mahrt of Oregon State University for their part in the experiment as well as Harry Stern of the University of Washington, who processed the turbulence data acquired by the sonic anemometer on the LongEZ. Work at the University of Washington Applied Physics Laboratory was supported by ONR (N00014-97-1-0278 and N00014-98-1-0189) and at JHU/APL by ONR (N00014-96-1-0376). Work at the NASA Laboratory for Hydrospheric Processes was also supported by ONR (N00014-97-1-0179) and by NASA's Office of Earth Science (RTOP 622-471000).

THE AUTHORS

PIERRE D. MOURAD is with the Applied Physics Laboratory of the University of Washington. His e-mail address is pierre@apl.washington.edu.

DONALD R. THOMPSON is at JHU/APL. His e-mail address is donald.thompson@jhuapl.edu.

DOUGLAS C. VANDEMARK is affiliated with the Laboratory for Hydrospheric Processes, NASA Goddard Space Flight Center. His e-mail address is dug@osb1.wff.nasa.gov.